


# Influence of diameter on high-pressure induced phase transitions in bismuth nanowire networks




Christopher Schröck <sup>\*</sup>

*GSI Helmholtz Center, Darmstadt, Germany*

*and Institute of Geosciences, Goethe University, Frankfurt am Main, Germany*

Ioannis Tzifas , Kay-Obbe Voss , Michael F. P. Wagner , and Christina Trautmann 

*GSI Helmholtz Center, Darmstadt, Germany*

Lkhamsuren Bayarjargal , Dominik Spahr , and Björn Winkler 

*Institute of Geosciences, Goethe University, Frankfurt am Main, Germany*

Maria Eugenia Toimil-Molares <sup>†</sup>

*GSI Helmholtz Center, Darmstadt, Germany*

*and Department of Materials and Geosciences, Technical University of Darmstadt, Darmstadt, Germany*



(Received 18 March 2025; revised 18 June 2025; accepted 23 June 2025; published 22 July 2025)

Size-dependent behavior of bismuth nanowire networks under high-pressure conditions was investigated at room temperature. Three-dimensional networks of freestanding interconnected bismuth nanowires with diameters between 34 and 85 nm were synthesized by electrodeposition in ion-track etched membranes, along with microcrystals as bulk analogues. Both types of samples were simultaneously compressed in diamond anvil cells under hydrostatic conditions up to 19.5 GPa. Synchrotron x-ray diffraction data reveal a shift of the Bi-I/-II, Bi-II/-III, and Bi-III/-V phase transition to higher-pressure values for decreasing nanowire diameter. In case of the thinnest wires, compression and decompression cycles revealed hysteresislike behavior of the shifts and a pronounced coexistence of the Bi-III and Bi-V phases upon compression. All samples exhibited bulklike compression behavior, as reflected in the evolution of their lattice parameter and bulk modulus. Only nanowires in the Bi-III phase showed a slightly reduced modulus compared to the corresponding bulk value. The systematic size dependence highlights the importance of excellent control on the geometrical parameters of the nanowires and consistent experimental conditions. The mechanical stability of the three-dimensional nanowire networks allowed the pressurization of samples of varying wire diameters under identical experimental conditions and facilitates systematic studies of size effects in nanomaterials with diameters as small as 10 nm.

DOI: [10.1103/c4fw-p99m](https://doi.org/10.1103/c4fw-p99m)

## I. INTRODUCTION

The phase behavior and properties of nanomaterials under compression have attracted great interest due to unique and often unexpected characteristics that do not manifest in their bulk counterparts [1,2]. The reduced dimensions in nanomaterials result in a larger ratio of surface-to-volume atoms and enhanced finite-size effects, directly affecting their intrinsic physical and chemical properties [2–5].

These properties depend on thermodynamic parameters such as pressure and temperature. Under compression, interatomic distances are reduced, which in turn affects the

thermodynamic stability [2,5]. However, since the energy balance of nanomaterials differs significantly from that of their bulk form, their high-pressure behavior can vary depending on the dimensions of the sample [3]. Consequently, the interplay between nanoscale dimensions and high-pressure conditions offers exciting opportunities for the discovery and exploration of novel structures and properties [2–4].

Nanomaterials are classified according to the number of sample dimensions that are below 100 nm [3]. Depending on whether one, two, or all three dimensions are below this threshold, the material is denoted as 2D (nanolayer), 1D (nanowire, NW), or 0D (nanoparticle), respectively [3]. There exists an extensive amount of studies on the high-pressure behavior of all kinds of nanomaterials, including modified stability ranges of polymorphs and significant shifts in phase-transition pressures (e.g., CdSe [6,7], CeO<sub>2</sub> [8], ZnO, and AlN [9]), as well as the formation of novel structures (e.g., TiO<sub>2</sub> [10–12], Si [13,14]).

To obtain reliable results on size-dependent properties in nanomaterials under high pressures, two key requirements must be met: (1) precise control of the size and geometry

<sup>\*</sup>Contact author: [c.schroeck@gsi.de](mailto:c.schroeck@gsi.de)

<sup>†</sup>Contact author: [m.e.toimilmolares@gsi.de](mailto:m.e.toimilmolares@gsi.de)

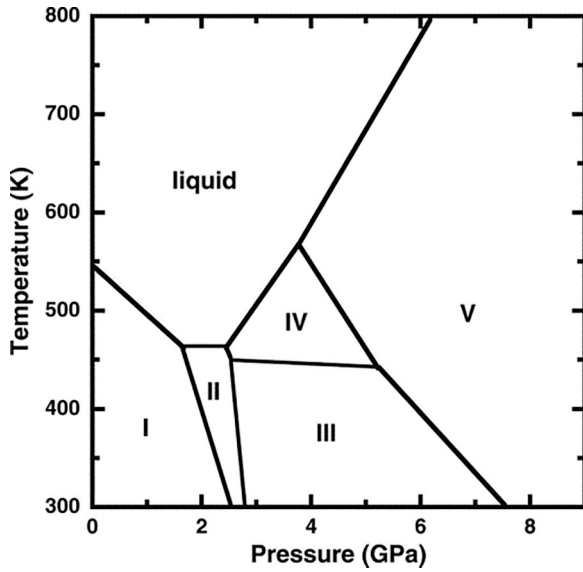


FIG. 1. Pressure-temperature phase diagram of bulk Bi, adapted from Ref. [22].

avoiding a broad size distribution and (2) a reliable experimental approach that ensures hydrostatic pressure conditions. If one of these conditions is not fulfilled, inconsistent and even contradictory results may be the consequence, as, for instance, reported in previous studies on nanosized silicon. For 1D and 0D silicon nanomaterials, the transition pressure decreased as the sample diameters became smaller [15,16], whereas increasing transition pressures were reported by other groups [14,17]. The comparison between these studies is challenging due to the rather wide diameter distribution of the investigated samples [16,17]. In addition, the experiments employed different pressure media and thus the pressure conditions significantly differed [17,18]. Another example is the investigation of  $\text{TiO}_2$ , which has a high-pressure phase that occurs only in nanoscale samples but not in bulk samples. For nanoparticles, the high-pressure phase was only found for particle diameters between 12 and 50 nm, whereas the same phase transformation was observed in nanowires with diameters greater than 100 nm [12,19]. Both examples underline the importance of well-defined sample dimensions and suitable experimental approaches in order to reveal and better understand the role of sample size in high-pressure phase transitions.

Here we present a systematic investigation of size-dependent phase transitions at room temperature of nanostructured bismuth (Bi) as a function of pressure, achieved by sample compression in diamond anvil cells (DACs) and structural analysis by using synchrotron x-ray diffraction (XRD). Bulk bismuth exhibits a rich polymorphism up to 9 GPa and has, to our knowledge, no further phase transitions up to at least 260 GPa [20,21]. The phase diagram is shown in Fig. 1 [22]. The corresponding high-pressure phases at room temperature along with their equilibrium transition pressures are summarized in Table I [20]. The crystal structure of the Bi-I, Bi-II, and Bi-V phase is trigonal, monoclinic, and cubic, respectively. Bi-III is best described as an incommensurate tetragonal host-guest structure [20,23,24]. The high-pressure

TABLE I. Transition pressures of different Bi phases at room temperature and respective space groups [20]. Bi-III is an incommensurate host(h)-guest(g) structure [23].

| Phase A $\rightarrow$ Phase B                           | Transition Pressure (GPa) |
|---|---------------------------|
| Bi-I ( $R\bar{3}m$ ) $\rightarrow$ Bi-II ( $C2/m$ )     | 2.60(1) <sup>a</sup>      |
| Bi-II $\rightarrow$ Bi-III (h: $I4/mcm$ , g: $I4/mmm$ ) | 2.75(1) <sup>a</sup>      |
| Bi-III $\rightarrow$ Bi-V ( $Im\bar{3}m$ )              | 8.5(1) <sup>a</sup>       |

<sup>a</sup>From Ref. [20].

characteristics of bulk bismuth have been the subject of various studies [20–22,25–28], whereas very little is known about the behavior of nanosized Bi [29].

We specifically focused on bismuth nanowire networks (Bi-NWNWs) with nanowire diameters  $d_{NW}$  of a few tens of nanometers, prepared by electrodeposition in track-etched polymer membranes [30–33]. The benefit of this technique is that the electrodeposited material adopts the exact shape and orientation of the host nanochannels. Thus, it enables a precise adjustment of the nanowire diameter, as well as of their relative orientation [33]. For our study, we synthesized three-dimensional interconnected NWNWs with different nanowire diameters. Their excellent mechanical stability allowed us to transfer multiple samples to the DAC. Compression of several nanosamples together with a micro-sized bulk sample in the same DAC has the additional advantage to characterize them independently but under identical hydrostatic conditions.

## II. METHODS

### A. Sample synthesis

All Bi samples investigated within this study were synthesized using electrodeposition of bismuth in nanochannels of track-etched polymer membranes [33,34]. The synthesis process involves four consecutive steps: (1) irradiation of polymer foils with high-energy heavy ions, (2) chemical etching of the ion tracks to obtain open nanochannels of diameter defined by the etching time, (3) electrodeposition of bismuth into the nanochannels, and (4) dissolution of the polymer template to release the polycrystalline nanowires (NWs). The ion irradiation was performed with  $\sim 2$  GeV gold ions at the universal linear accelerator (UNILAC) at the GSI Helmholtz Center for Heavy Ion Research in Darmstadt, Germany. As templates, 30  $\mu\text{m}$  thick polycarbonate foils were exposed to the ion beam from four different directions, each oriented  $90^\circ$  relative to the neighboring directions while maintaining a constant angle of beam incidence of  $45^\circ$  to the sample surface. Chemical etching of the irradiated templates leads to a network of interconnected nanochannels, with channel diameters adjusted by the applied etching time. For the synthesis of Bi microcrystals, polycarbonate templates with parallel-oriented nanochannels were used. In this case, the ion-beam incidence was normal to the polymer surface and etching was performed for 480 s, resulting in pores of approximately 200 nm diameter.

Electrodeposition of Bi inside the pores was achieved using a three-electrode setup and a customized aqueous 0.1 M

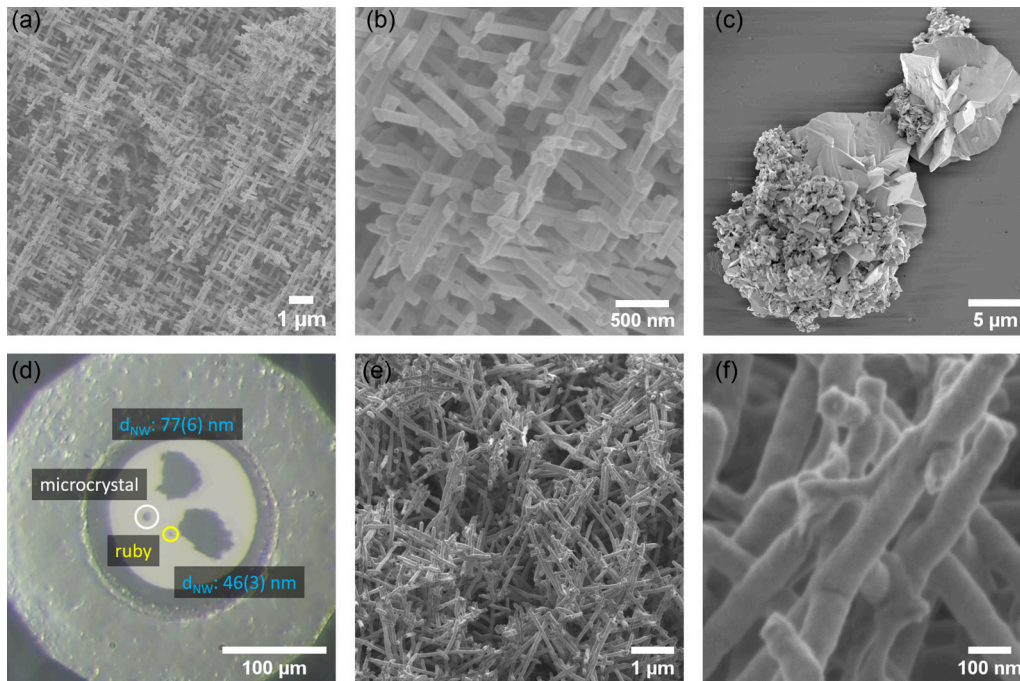


FIG. 2. Representative SEM images of Bi-NWNWs in (a) low and (b) high magnification. (c) Top-view SEM image of the polymer template, showing a Bi microcrystal obtained by extending electrodeposition times by 400 s after pore filling. (d) Optical microscopy image of our diamond anvil cell loaded with two different bismuth NWNWs, a microcrystal (as bulk sample) and a ruby (as pressure gauge). Recovered NWNW after compression up to 11 GPa at (e) low and (f) high magnification.

Bi-electrolyte solution [30]. Pulsed potentials were applied with an on-potential of  $-180$  mV for 20 ms and an off-potential set to  $-140$  mV for 100 ms relative to a Ag/AgCl (saturated KCl) reference electrode [30]. For the NWNWs, the deposition was stopped once the channels were completely filled (see Appendix A, Fig. 9). Representative scanning electron microscopy (SEM) images of the synthesized Bi-NWNWs in (a) low and (b) high magnification are displayed in Fig. 2. The low magnification image illustrates the high degree of interconnectivity. Overall, the wire growth is homogeneous, the diameters appear constant along their entire wire length, and a mechanically stable nanostructure with interconnected NWs is obtained. The high magnification image shown in Fig. 2(b) displays individual NWs of cylindrical shape and smooth surfaces. The mean nanowire diameter  $d_{NW}$  was determined by evaluating a total of 40 individual NWs from SEM images of at least four different, arbitrarily selected areas per sample, yielding nanowires of 34(3) nm, 46(3) nm, 77(6) nm, and 85(5) nm in diameter, corresponding to a track-etching time of 90 s, 120 s, 180 s, and 240 s, respectively. The given uncertainties correspond to the standard deviation. Significant amounts of impurities and the presence of nanovoids in the nanowires can be excluded based on scanning transmission electron microscopy and energy-dispersive x-ray spectrometry, that were performed in a different context (not shown here) [35,36].

For the synthesis of the microcrystals, the electrodeposition process was extended by additional 400 s after pore filling, resulting in the growth of microcrystals on top of the template surface (see Appendix, Fig. 9). These microcrystals were transferred to the DACs individually by picking them directly from the surface of the template. Their diameters ranged

from 5  $\mu$ m to a few tens of micrometers. Figure 2(c) shows a typical SEM image of two adjacent Bi microcrystals on top of the template. Their faceted surfaces indicate a multigrain assembly with large crystallites. Further details regarding the synthesis procedure can be found in Appendix A.

## B. High-pressure experiments

The samples were compressed using gas-loaded custom-built Boehler-Almax plate DACs equipped with Boehler-Almax diamond anvils (type Ia and IIas) with culets of either 300  $\mu$ m or 350  $\mu$ m in diameter [37]. Metal gaskets made of stainless steel or tungsten were indented to a thickness of 55(5)  $\mu$ m and the holes drilled into them had a diameter of 130(5)  $\mu$ m. Gas loading was performed using neon or argon gas as pressure transmitting medium (PTM), for compression up to a maximum of 20 and 12 GPa, respectively. This takes into account the hydrostatic limits of the respective PTM and ensures that the standard deviation of the pressure within the gasket hole does not exceed 0.2 GPa [18]. Networks with different nanowire diameters were placed inside the same DAC, to be compressed simultaneously within one experimental run. In addition, a Bi microcrystal was loaded as bulk reference along with a small ruby crystal serving as a pressure gauge. Figure 2(d) shows a photo of the sample chamber of one of the DACs loaded with three different samples and a ruby crystal. During characterization, the samples were identified by their specific positions and shapes. As the sample shapes did not change during the experiment, bridging of the samples between the diamonds can be excluded. Some NWNW samples were recovered after decompression and investigated using SEM. The sample shown in Figs. 2(e) and



2(f) was compressed up to a maximum pressure of 11 GPa and therefore sequentially transformed to the Bi-II, Bi-III, and Bi-V phases. After the compression and decompression procedure, the shape and dimension of the recovered NWNWs including the interconnections were preserved. The reduced regularity and the increased number of broken nanowires that are observed may be related to the sample handling during transfers.

Measurements of pressure-volume data were conducted at room temperature using synchrotron x-ray diffraction (XRD) at the extreme conditions beam line P02.2 at PETRA-III, DESY Hamburg, which provides a beam of 42.7 keV (wavelength 0.2904 Å) and a spot size of  $8 \times 3 \mu\text{m}^2$  on the sample [38]. Data acquisition was performed using a PerkinElmer XRD1621 detector, calibrated with a  $\text{CeO}_2$  powder standard and analyzed using the software DIOPTAS [39]. To ensure equilibration, each pressure point was manually set and held for at least 30 min before sample characterization. Pressures were determined by ruby fluorescence before and after characterization. Data evaluation involved the software packages DIOPTAS [39] and GSAS-II [40]. For each pressure point, the volume per atom,  $V$ , was deduced from the diffraction data of at least two measurements, primarily using the Rietveld method. In individual cases, data of lower quality required the use of the LeBail method instead. Whenever applicable, the diffraction signals of the pressure-transmitting medium were also refined and the pressure  $p$  was determined based on the respective equation of state (EoS) [41,42]. This allowed verification of the pressures determined on the basis of ruby fluorescence during the experiment. The obtained pressure and volume data were then fitted applying the Birch-Murnaghan equation (see Eq. (1) [43,44]) in order to determine the bulk modulus  $K_0$  and the ambient pressure reference volume  $V_0$ ,

$$p = \frac{3}{2}K_0 \left[ \left( \frac{V_0}{V} \right)^{\frac{7}{3}} - \left( \frac{V_0}{V} \right)^{\frac{5}{3}} \right] \times \left\{ 1 + \frac{3}{4}(K'_0 - 4) \left[ \left( \frac{V_0}{V} \right)^{\frac{2}{3}} - 1 \right] \right\}. \quad (1)$$

The second term in Eq. (1) also includes the derivative of the bulk modulus with respect to pressure, denoted as  $K'_0$ . It is challenging to include  $K'_0$  as a free parameter to the fitting because the stability range of the bismuth phases are narrow and hence the number of available experimental data points is too small for applying a third-order fit with three free parameters. However, Eq. (1) can be further simplified by assuming  $K'_0 = 4$ , which is a reasonable estimate for many substances and compression within a limited pressure range [45,46]. This yields a second-order equation as shown in Eq. (2) with  $K_0$  and  $V_0$  as free parameters. All EoS fits were performed using the software EOSFIT7 [47],

$$p = \frac{3}{2}K_0 \left[ \left( \frac{V_0}{V} \right)^{\frac{7}{3}} - \left( \frac{V_0}{V} \right)^{\frac{5}{3}} \right]. \quad (2)$$

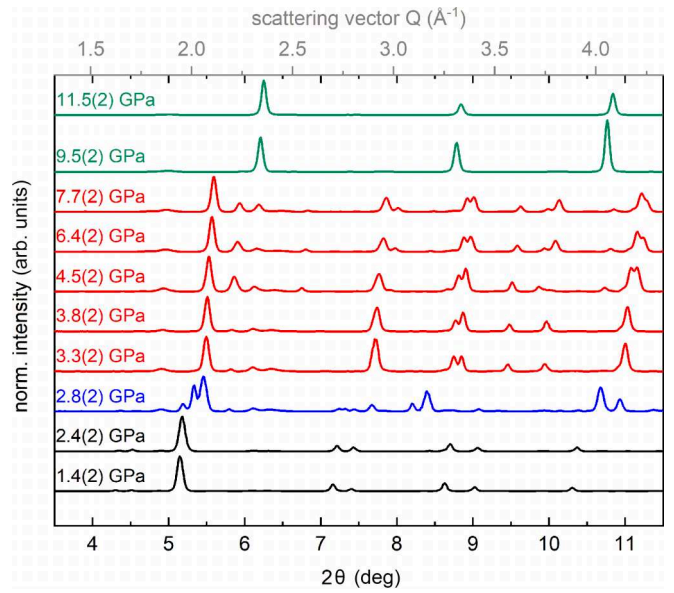


FIG. 3. Stacked XRD data of a Bi microcrystal that was stepwise pressurized up to 11.5 GPa. High-pressure phases Bi-I, Bi-II, Bi-III, and Bi-V are indicated in black, blue, red, and green, respectively. The diffractograms were normalized to the reflection of highest intensity at highest pressure within the same phase. PTM: Ar; wavelength 0.2904 Å.

### III. RESULTS AND DISCUSSION

#### A. Phase transitions of pressurized Bi microcrystals

Figure 3 shows a series of diffractograms collected during compression of a Bi microcrystal. Each high-pressure phase can be identified by a characteristic set of reflections. The diffractograms are colored in black, blue, red, and green, referring to the Bi-I, Bi-II, Bi-III, and Bi-V phase, respectively. This compression run reveals transitions from 2.4 to 2.8 GPa, 2.8 to 3.3 GPa, and 7.7 to 9.5 GPa, attributed to the respective phase transition from Bi-I to Bi-II, Bi-II to Bi-III, and Bi-III to Bi-V. Multiple compression experiments on various microcrystals were performed. The evaluated volumes per atom plotted versus the respective pressures are presented in Fig. 4. The data from different compression runs show excellent consistency. Taking all measurements into account, the transition pressures of the bulk samples can be refined to 2.65(20) GPa (Bi-I to Bi-II), 2.8(2) GPa (Bi-II to Bi-III), and 8.8(4) GPa (Bi-III to Bi-V). These values are indicated by the dashed lines in Fig. 4 and are arithmetic means of the pressures of the two data points closest to the transition, regardless of the respective experimental run. The reported errors represent either the size of the pressure gap or the uncertainty in pressure determination with a minimum value of  $\pm 0.2$  GPa. Notably, the transitions from Bi-I to Bi-II and from Bi-II to Bi-III are accompanied by a significant decrease in the volume per atom, which is less pronounced in the case of the transition from Bi-III to Bi-V. The transition pressures and volumes of the microcrystals obtained in this way closely align with the literature values [20], demonstrating that Bi microcrystals are suitable as a bulk reference material. Unless otherwise stated,

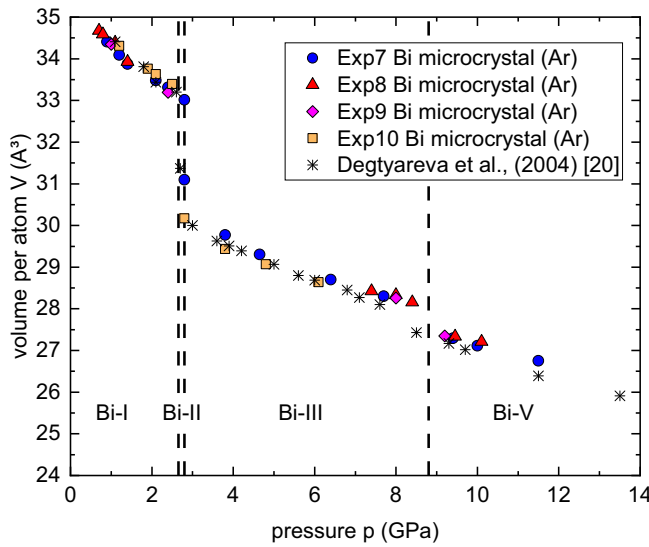


FIG. 4. Volume per atom,  $V$ , at room temperature as a function of pressure  $p$  for Bi microcrystals and values from Degtyareva *et al.* [20] for comparison. The black dashed lines represent the transition pressures, as defined by the arithmetic mean of the pressures of the two data points closest to the transition, regardless of the experimental run. The PTM is indicated in brackets.

all comparisons to bulk samples are therefore referred to the microcrystals.

### B. Phase transitions of pressurized bismuth nanowire networks

The volumes per atom obtained from compression runs on Bi-NWNWs with nanowires of various diameters are shown in Fig. 5. From top to bottom, the plots display samples with nanowire diameters  $d_{NW}$  of 85(5) nm, 77(6) nm, 46(3) nm, and 34(3) nm. The data of all individual experimental runs are highly consistent and show that the volume per atom continuously decreases with increasing pressure, regardless of the used PTM. Similar to the microcrystals, the phase transitions from Bi-I to Bi-II and Bi-II to Bi-III are accompanied by a significant decrease in the volume per atom, whereas the change for the transition from Bi-III to Bi-V is less pronounced. As above, the respective transition pressures are indicated by dashed lines.

All NWNW samples with the exception of the 85(5) nm diameter nanowires exhibit the expected sequence of the high-pressure phases, consistent with the findings for the microcrystal samples. The phase transitions from Bi-I to Bi-II are observed between 2.8(2) and 3.1(2) GPa, slightly above the bulk transition pressure of 2.65(20) GPa. For the 85(5) nm nanowires, the Bi-II phase is not present in any of the achieved pressure points. This phase is probably skipped due to the narrow pressure range in which the phase is stable [20]. Upon further compression, transformation to the Bi-III phase is found at pressures between 3.5(2) GPa and 3.7(2) GPa in all NWNW samples. These pressures are also elevated, compared to the respective transition pressure in the bulk samples at 2.9(2) GPa. In some cases during the transitions to the Bi-II and Bi-III phase, a coexistence of the initial and new phases is present. However, the transition is already completed

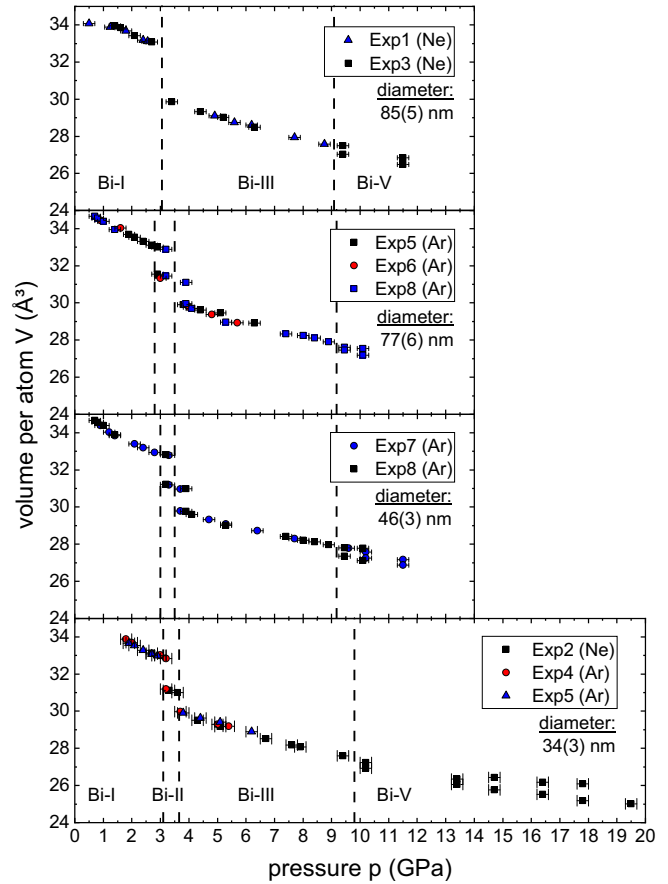


FIG. 5. Volume per atom,  $V$ , at room temperature as a function of pressure for Bi nanowires with diameters  $d_{NW}$  of 85(5) nm, 77(6) nm, 46(3) nm, and 34(3) nm. The vertical dashed lines represent the transition pressures, defined as the midpoint of the final pressure step in which the new phase first emerged. The PTM is indicated in brackets.

at the subsequent pressure point. In the case of the phase transition from Bi-III to Bi-V, the transition pressures of the NWNW samples range from 9.1(4) GPa to 9.8(4) GPa. In contrast, the Bi-V phase already appears in microcrystals at 8.8(4) GPa. Additionally, a pronounced coexistence of the Bi-III and Bi-V phases occurs in the NWNW samples and complete transformation is not achieved up to 12.0 GPa in any of the investigated networks. The sample with the thinnest nanowires [34(3) nm] was selected for further compression. As shown in Fig. 5, Bi-III contributions are present up to a pressure of 17.8(2) GPa and the transformation is completed at 19.2(2) GPa. This is in contrast to the behavior of the bulk samples, whose phase transformations are completed within a narrower pressure range.

The derived phase-transition pressures as a function of the inverse wire diameter are summarized in Fig. 6. The error bars reflect the size of the pressure step during which the transition occurred. Compared to the bulk samples, the transition pressures for NWNWs show a clear and significant shift to higher values depending on the nanowire diameter and phase. Among all transitions, the Bi-III to Bi-V transition exhibits the largest absolute pressure shift for the thinnest nanowires

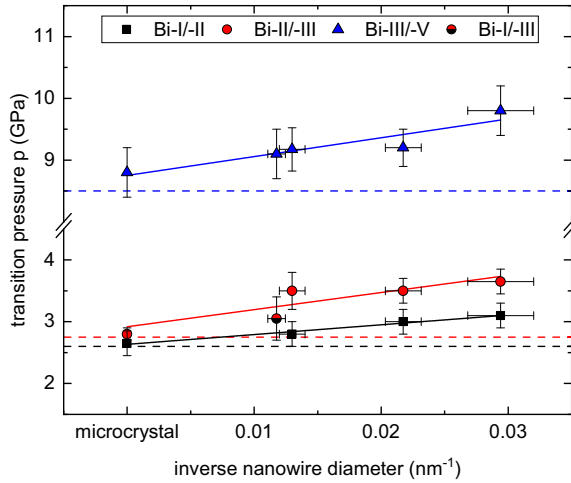


FIG. 6. Transition pressures at room temperature of Bi-NWNWs and microcrystals. The horizontal dashed lines correspond to bulk transition values reported in the literature [20]. Solid lines are fits based on Eq. (3) with parameters summarized in Table II. Bi-I/-III represents the data of the experiment, where the Bi-II phase was skipped.

with  $\Delta p = 1.0$  GPa, which corresponds to a relative increase of 11 %. The relative changes are even more pronounced for the phase transitions from Bi-I to Bi-II (12 %) and Bi-II to Bi-III (27 %), though these changes are similar across all investigated diameters.

To quantify the influence of the nanowire diameter  $d_{NW}$  on the pressure shift, Eq. (3) was applied, where  $p$  and  $p_0$  represent the phase-transition pressure of the nanowires and the bulk, respectively [9,48]. The linear coefficient  $k$  comprises contributions of surface energy, surface stress, and the dimensionality of the sample [9]. Applying Eq. (3) to the transition pressures of the NWNWs summarized in Fig. 6 yields  $k$  values of  $-16(2)$ ,  $-28(9)$ , and  $-30(7)$  GPa nm, for the Bi-I/-II, Bi-II/-III, and Bi-III/-V phase transition, respectively. The values are in the same order of magnitude, albeit with smaller absolute values, as in the case of ZnO ( $k = -56.13$  GPa nm) and AlN ( $k = 68.92$  GPa nm) nanopowders [9]. Therefore, a less-pronounced diameter dependence is present in the case of the nanowires, which can be explained by the higher dimensionality of their geometry [1,3,9],

$$p = p_0 - k \left( \frac{1}{d_{NW}} \right). \quad (3)$$

To further assess the high-pressure characteristics of the NWNW samples, the bulk moduli  $K_0$  and the ambient pressure

TABLE II. Results from fitting the size-dependent shifts in transition pressures (data displayed in Fig. 6) using Eq. (3).

|            | Pressure $p_0$<br>(GPa) | Linear coefficient $k$<br>(GPa nm) | $R^2$ |
|------------|-------------------------|------------------------------------|-------|
| Bi-I/-II   | 2.6(1)                  | $-16(2)$                           | 0.98  |
| Bi-II/-III | 2.9(2)                  | $-28(9)$                           | 0.84  |
| Bi-III/-V  | 8.8(1)                  | $-30(7)$                           | 0.86  |

reference volumes  $V_0$  were determined for the phases Bi-I, Bi-III, and Bi-V, while noting that the number of data points for the analysis of Bi-II is too small. A second-order Birch-Murnaghan fit was applied [see Eq. (2)] and the volumes per atom obtained from individual experiments are summarized and fitted (Table III). For the Bi-I phase, all samples regardless of their nanowire diameter show consistent ambient pressure reference volumes  $V_0$  and bulk moduli  $K_0$ . The average values of  $\bar{V}_0 = 35.2(2) \text{ \AA}^3$  and  $\bar{K}_0 = 38.5(52) \text{ GPa}$  are in good agreement with both bulk references [20]. The same good agreement applies to nanowire samples in the Bi-III phase. The reference volumes only reveal minor deviations from their average value of  $\bar{V}_0 = 31.9(2) \text{ \AA}^3$  and the respective bulk reference values. The deduced average bulk modulus is  $\bar{K}_0 = 49(4) \text{ GPa}$ , which closely aligns with the bulk reference value. However, there is one outlier indicating a significantly larger bulk modulus than the other samples (value labeled by an asterisk). Excluding this outlier, the average bulk modulus drops to  $\bar{K}_0 = 46(3) \text{ GPa}$ , which is slightly lower than that of the bulk reference. In the Bi-V phase, the analysis was limited to the thinnest nanowires due to an insufficient amount of data for the other samples. In this case, most of the considered data points are not a pure Bi-V phase, but a mixture with Bi-III. The bulk moduli of the NWNWs in the Bi-V phase agree with the literature [20]. Notably, there is a significant discrepancy between the results obtained from second-order and third-order fits for the Bi-V phase, which was not observable for the Bi-I and Bi-III phases in the case of third-order fits with partially fixed parameters. Although both values coincide with the respective literature value, the bulk moduli  $K_0$  deviate by 12 GPa. Overall, the ambient pressure reference volumes  $V_0$  of all phases and samples show excellent agreement with the values of the bulk samples. Only NWNWs in the Bi-III phase reveal slightly lower bulk moduli  $K_0$  than the bulk references [20]. Within the investigated range, a systematic dependence of the bulk modulus on the diameter is not apparent.

The bulk modulus of the Bi-V phase has been the subject of several previous studies. The most recent publication on the widest pressure range to date reports a bulk modulus of  $K_0 = 38.2 \text{ GPa}$  with  $K'_0 = 5.8$  and  $V_0 = 31.7 \text{ \AA}^3$  [21]. This value is significantly smaller than the results obtained here and by Degtyareva *et al.* [20], but agrees very well with another study from Akahama *et al.* [49]. The works from Campbell *et al.* [21] and Akahama *et al.* [49] have in common that the investigated pressure range exceeded 200 GPa and that bismuth foils were used as the sample. However, the question of whether the considerably larger pressure range or the alternative sample geometry is responsible for the large deviation cannot be resolved in this context. Liu *et al.* [50] investigated a polycrystalline bismuth sample of  $60 \mu\text{m}$  up to a maximum pressure of 55 GPa. Depending on whether a second- or third-order Vinet-type EoS fit was applied, the resulting bulk moduli are either  $K_0 = 52.6 \text{ GPa}$  or  $K_0 = 41 \text{ GPa}$  with  $K'_0 = 5.4$ , respectively. This strong dependence on the fit order was also found in the present work in the case of the Bi-V phase, indicating the sensitivity of the bulk modulus on the applied fit and the number of fixed parameters [21,50]. Therefore, the deviation may be attributed to the fitting routine applied or the specific characteristics of the sample used by Liu *et al.* [50], but the limited sample description does not

TABLE III. Bulk moduli  $K_0$  and ambient pressure reference volumes  $V_0$ . Unless otherwise stated, second-order Birch-Murnaghan fits [ $K'_0 = 4.0$ , see Eq. (2)] were applied.

| Diameter $d_{NW}$<br>(nm) | Bi-I                       |                | Bi-III                     |                    | Bi-V                       |                      | $K'_0$              |
|---------------------------|----------------------------|----------------|----------------------------|--------------------|----------------------------|----------------------|---------------------|
|                           | $V_0$<br>(Å <sup>3</sup> ) | $K_0$<br>(GPa) | $V_0$<br>(Å <sup>3</sup> ) | $K_0$<br>(GPa)     | $V_0$<br>(Å <sup>3</sup> ) | $K_0$<br>(GPa)       |                     |
| 34(3)                     | 35.3(3)                    | 37(6)          | 32.3(2)                    | 43(2)              | 30.3(3)                    | 30.7(4) <sup>a</sup> | 5.2(9) <sup>a</sup> |
| 46(3)                     | 35.2(1)                    | 38(3)          | 31.5(2) <sup>b</sup>       | 58(5) <sup>b</sup> |                            |                      |                     |
| 77(6)                     | 35.3(1)                    | 37(4)          | 32.0(2)                    | 49(3)              |                            |                      |                     |
| 85(5)                     | 35.0(2)                    | 42(7)          | 31.8(2)                    | 47(3)              |                            |                      |                     |
| microcrystal              | 35.2(1)                    | 39(4)          | 31.5(3)                    | 55(7)              |                            |                      |                     |
| bulk [20]                 | 35.375(3)                  | 38.2(5)        | 31.5(4)                    | 53(1)              | 30.3(2)                    | 30.8(4) <sup>a</sup> | 4.5(5) <sup>a</sup> |

<sup>a</sup>Based on a third-order Birch-Murnaghan fit [see Eq. (1)].

<sup>b</sup>Outlier; see discussion.

permit further conclusions. A more comprehensive comparison of the results obtained from different fitting approaches is provided in the Supplemental Material [51].

To further evaluate the compression behavior of all our samples, the corresponding  $c/a$  ratios of the Bi-I, Bi-II, and

Bi-III phases are plotted in Figs. 7(a) and 7(b), respectively. Both, NWNWs and microcrystals follow the same trend, coinciding with the bulk reference from the literature [20]. In the Bi-I phase, the  $c/a$  ratios show a continuous decrease, indicating a more pronounced compression along the crystallographic  $c$  axis. In contrast, the  $c/a$  ratios in the Bi-II and Bi-III phases do not show a pressure dependence, but scatter around a constant average value of  $c/a = 0.494(2)$  and  $0.488(2)$ , respectively.

### C. Decompression of Bi nanowire networks

For the network sample with the smallest nanowire diameter [ $d_{NW} = 34(3)$  nm], the volume per atom was also evaluated during decompression. The results are plotted in Fig. 8 along with the respective compression data (Exp5 in Fig. 5, bottom). For comparison, the corresponding data for bulk bismuth from Degtyareva *et al.* [20] are included as black stars. During decompression, starting from the Bi-V phase,

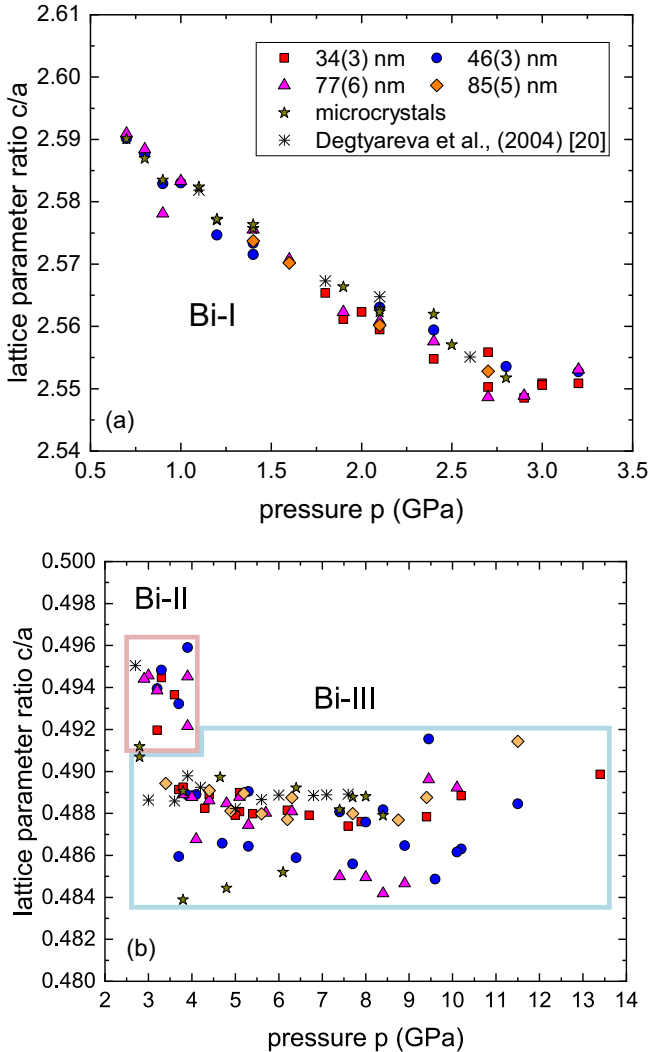


FIG. 7. Lattice parameter ratio  $c/a$  as a function of pressure for samples in the (a) Bi-I phase and (b) Bi-II (red frame) and Bi-III (blue frame) phases.

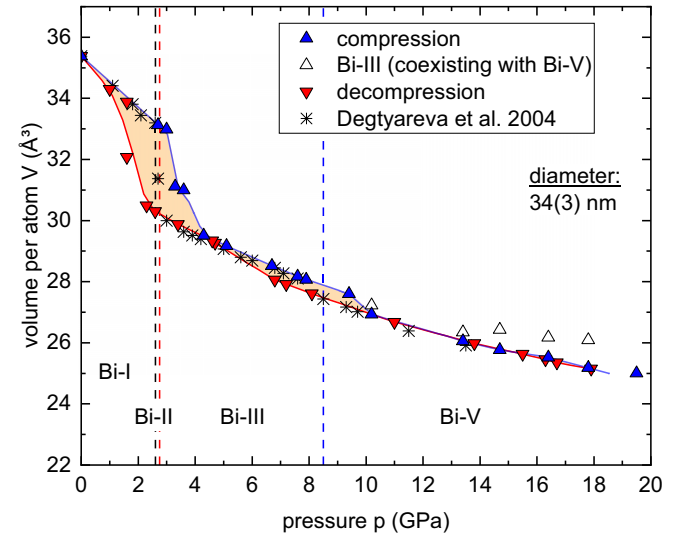


FIG. 8. Volume per atom,  $V$ , at room temperature of Bi-NWNWs of 34(3) nm in diameter during compression and decompression (PTM: Ne). Lines are guides to the eye and filled areas highlight the hysteresis. Vertical lines and labels indicate transition pressures in bulk samples. Data from Degtyareva *et al.* [20] display bulk Bi during compression.



TABLE IV. Geometrical parameters of the prepared samples. The number of pores refers to the number of ions the template was exposed to and are identical to the number of NWs.

| Sample type  | No. of pores<br>(1/cm <sup>2</sup> ) | Angle of irradiation<br>(deg) | Etching time<br>(s) | Nanowire diameter $d_{NW}$<br>(nm) |
|--------------|--------------------------------------|-------------------------------|---------------------|------------------------------------|
| network      | $4 \times 5 \times 10^9$             | 45                            | 90                  | 34(3)                              |
| network      | $4 \times 5 \times 10^9$             | 45                            | 120                 | 46(3)                              |
| network      | $4 \times 5 \times 10^8$             | 45                            | 180                 | 77(6)                              |
| network      | $4 \times 5 \times 10^8$             | 45                            | 240                 | 85(5)                              |
| microcrystal | $1 \times 10^6$                      | 90                            | 480                 | -                                  |

the cubic high-pressure phase remains stable until a pressure of 6.8(2) GPa. Below 4.7(2) GPa, the pure Bi-III phase is observed down to a pressure of 2.3(2) GPa. The subsequent decompression step results in a mixed Bi-II and Bi-I phase at 1.6(2) GPa, followed by a transition to a pure Bi-I phase at 1.0(2) GPa.

All transitions during decompression reveal significant shifts to lower pressures. There is a pressure shift of 1.7 GPa compared to the Bi-III to Bi-V phase transition, while the Bi-II and Bi-I phases are also first detected at 0.9 GPa below the Bi-I to Bi-II transition. Pronounced coexistence, as seen during compression, cannot be identified. The results suggest a hysteresislike behavior around the respective phase-transition pressures, as highlighted by the filled area in Fig. 8. This supports the existence of a size effect in Bi-NWNWs resulting in enhanced phase stability.

#### IV. CONCLUSIONS

This study successfully explored the size-dependent behavior of bismuth under high-pressure conditions at room temperature, comparing both bulk and nanostructured samples. Three-dimensional freestanding networks of bismuth nanowires with tailored diameters between 34 nm and 85 nm, as well as microcrystals, were synthesized by electrodeposition and characterized under simultaneous compression. All investigated nanowire samples displayed bulk-like compression behavior, reflected in their bulk moduli and lattice parameter evolution during compression. Notably, only the nanowires in the Bi-III phase showed slightly reduced bulk moduli. An extended coexistence range of the Bi-III and Bi-V phases was revealed upon compression in the case of the sample having the thinnest diameter. As the nanowire diameter decreased, transition pressures during compression increased, while those during decompression decreased, indicating a size-dependent, hysteresislike shift in transition pressures.

Throughout the compression and characterization process, the structure and dimensions of the freestanding nanowire networks remained stable. The methodology demonstrated in this work enables detailed systematic investigations of the high-pressure behavior of nanowires and is applicable to a variety of materials and nanowire diameters down to 10 nm, enabling further systematic studies across a broad size range.

#### ACKNOWLEDGMENTS

We acknowledge GSI (Darmstadt, Germany) and DESY (Hamburg, Germany), both members of the Helmholtz

Association HGF, for the provision of experimental facilities. The fabrication of nanowires is based on UMAT experiments performed at the X0-beamline of the UNILAC at GSI in the framework of FAIR Phase-0. The beam times for the XRD analysis were carried out at PETRA III on beam line P02.2 allocated for Proposals No. I-20220591 and No. I-20231391. We would like to thank Timofey Fedotenko and Konstantin Glazyrin for their assistance in using the P02.2 beam line. B.W., L.B., and D.S. gratefully acknowledge funding from the DFG (Projects No. WI1232, No. BA4020, and No. BY101/2-1). C.S. acknowledges financial support from the Helmholtz Graduate School HGS-HIRE. This work has been funded via the R&D program of the GSI Helmholtz Center for Heavy Ion Research.

#### DATA AVAILABILITY

The data that support the findings of this article are not publicly available. The data are available from the authors upon reasonable request.

#### APPENDIX A: TEMPLATE AND SAMPLE SYNTHESIS

Sample synthesis is based on a four-step process: (1) ion irradiation of polymer foils, (2) selective etching of ion tracks, (3) electrodeposition of polycrystalline bismuth into the pores, and (4) dissolution of the polymer template.

##### 1. Ion Irradiation and Track Etching

Polycarbonate foils of 30  $\mu\text{m}$  thickness were irradiated with gold ions of 2.2 GeV kinetic energy, provided by the universal linear accelerator (UNILAC) at GSI Helmholtz Center for Heavy Ion Research GmbH in Darmstadt, Germany. The ion energy was sufficiently high for the ions to pass through the entire polymer foil. This creates a cylindrical track along the ion trajectory composed of damaged material. The diameters of the tracks range from 5 to 10 nm, depending on the type of material. Templates used for the synthesis of microcrystals were irradiated under normal incidence, whereas templates used for NWNWs were irradiated with an incidence angle of 45° from four different directions. In the latter case, each direction is rotated by an angle of 90° relative to its neighboring direction, resulting in ion tracks intersecting in relative angles of 90°, all revealing an angle of 45° to the foil surface.

##### 2. Selective Etching of Ion Tracks

Cylindrical pores (nanochannels) are produced by selective etching of the ion tracks using 6 M sodium hydroxide solution at 50 °C. The nanochannel diameters were adjusted by



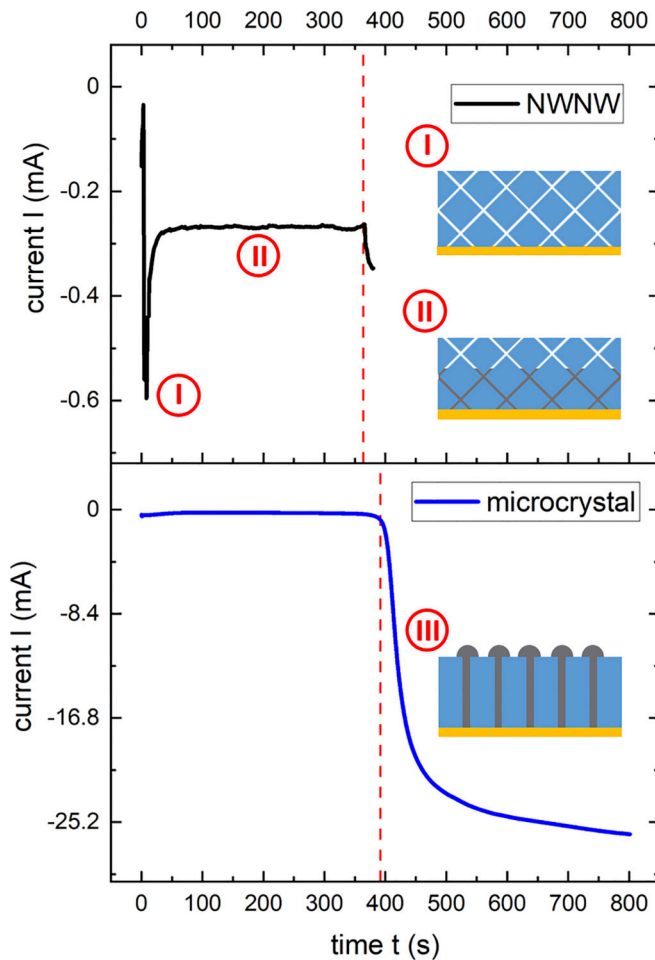


FIG. 9. Typical current-time curves for the electrodeposition of a NWNW (top) and microcrystal (bottom). Dashed lines indicate the estimated onset time for pore filling, which determined the termination of the deposition time in the case of the NWNW. Sketches on the right display the filling status of the respective section.

applying various etching times, assuming a constant etching rate of  $23(2) \text{ nm min}^{-1}$ . After etching, the templates were thoroughly rinsed in deionized water. Template properties and etching times are summarized in Table IV. For the synthesis of NWNWs, templates with interconnected nanochannels were used. For nanowire diameters greater than 70 nm, the number of nanochannels in the template was reduced by a factor of 10 to minimize overlapping effects.

### 3. Electrodeposition

First, a conductive backelectrode was applied to one side of the template, by sputter deposition of gold (approximately 100 nm), subsequently reinforced to a thickness of 1  $\mu\text{m}$  by galvanostatic deposition of Au using a commercial AuSF electrolyte (Metakem GmbH, Germany). Electrodeposition of Au was performed at room temperature applying a current density of  $-4 \text{ mA cm}^{-2}$ . This backelectrode closes the pores from one side while providing a mechanically stable substrate.

Polycrystalline bismuth was deposited inside the pores employing pulsed deposition and a three-electrode setup. The Au backelectrode serves as the working and a Pt wire as the

counter electrode. The onset and offset potential were set to  $-180 \text{ mV}$  for 20 ms and  $-140 \text{ mV}$  for 100 ms vs Ag/AgCl (saturated KCl) reference electrode, respectively. The aqueous Bi electrolyte was composed of  $31.6 \text{ gL}^{-1}$  bismuth(III) chloride,  $78.6 \text{ mL}^{-1}$  glycerol,  $162.4 \text{ mL}^{-1}$  hydrochloric acid fuming 37%,  $11.2 \text{ gL}^{-1}$  sodium chloride,  $45.2 \text{ gL}^{-1}$  tartaric acid, and  $1.0 \text{ mL}^{-1}$  surfactant Dowfax 2a1 (DOW Deutschland Anlagengesellschaft mbH, Germany). Electrodeposition of the Bi-NWNWs was terminated as soon as there was an increase in the deposition current, indicating the completion of the template filling. In the case of the Bi microcrystals, the deposition time was extended from this point on for another 400 s. In this way, the electrodeposition continued outside the pores, forming microcrystals up to a few tens of micrometers in diameter. Typical deposition curves (current  $I$  over time  $t$ ) are shown in Fig. 9. The strong current increase after pore filling is due to the increase of electrochemically active surface area for the deposition of Bi.

### 4. Dissolution of Polymer Template

Microcrystals were picked directly from the surface, whereas the release of the NWNWs required dissolution of the polycarbonate template in dichloromethane (DCM) (Carl Roth GmbH + Co. KG, Germany). For this, the NWNWs were mounted in customized holders and immersed in DCM for at least 24 h. In order to remove any polymer residuals, the DCM was exchanged up to five times. Finally, all samples were checked using scanning electron microscopy.

### APPENDIX B: COMPRESSED BI-NWNWs (Exp2)

Figure 10 displays the XRD data of Bi-NWNWs with wire diameters of  $34(3) \text{ nm}$  (Exp2) at different pressures.

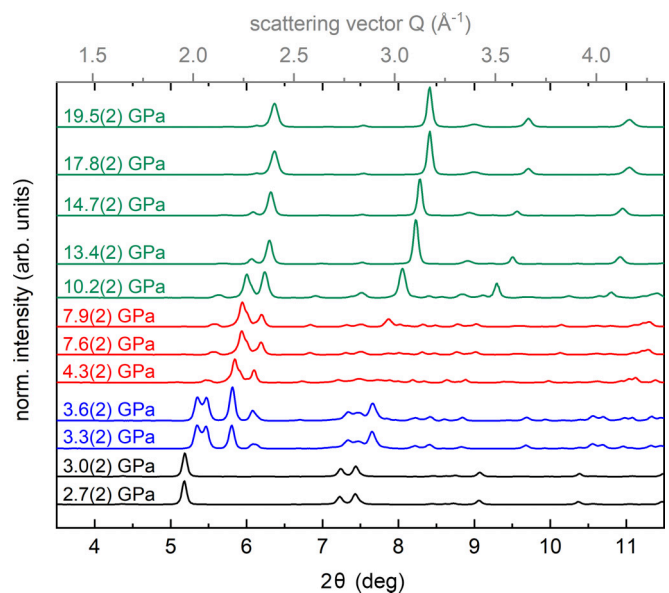


FIG. 10. Stacked XRD data of the Bi-NWNW of  $d_{\text{NW}} = 34(3) \text{ nm}$  compressed at room temperature (Exp2, Fig. 5). High-pressure phases Bi-I, Bi-II, Bi-III, and Bi-V are indicated in black, blue, red, and green, respectively. The diffractograms are normalized to the reflection of highest intensity at highest pressure within the same phase. PTM: Ne; wavelength 0.2904 nm.

- [1] E. Roduner, Size matters: Why nanomaterials are different, *Chem. Soc. Rev.* **35**, 583 (2006).
- [2] L. Meng, T. Vu, L. Criscenti, T. Ho, Y. Qin, and H. Fan, Theoretical and experimental advances in high-pressure behaviors of nanoparticles, *Chem. Rev.* **123**, 10206 (2023).
- [3] A. San-Miguel, Nanomaterials under high-pressure, *Chem. Soc. Rev.* **35**, 876 (2006).
- [4] D. Machon, V. Pischedda, S. Le Floch, and A. San-Miguel, Perspective: High pressure transformations in nanomaterials and opportunities in material design, *J. Appl. Phys.* **124**, 160902 (2018).
- [5] F. Bai, K. Bian, X. Huang, Z. Wang, and H. Fan, Pressure induced nanoparticle phase behavior, property, and applications, *Chem. Rev.* **119**, 7673 (2019).
- [6] S. Tolbert and A. Alivisatos, Size dependence of a first order solid-solid phase transition: The wurtzite to rock salt transformation in CdSe nanocrystals, *Science* **265**, 373 (1994).
- [7] S. Tolbert and A. Alivisatos, The wurtzite to rock salt structural transformation in CdSe nanocrystals under high pressure, *J. Chem. Phys.* **102**, 4642 (1995).
- [8] B. Liu, M. Yao, B. Liu, Z. Li, R. Liu, Q. Li, D. Li, B. Zou, T. Cui, G. Zou *et al.*, High-pressure studies on CeO<sub>2</sub> nanooctahedrons with a (111)-terminated surface, *J. Phys. Chem. C* **115**, 4546 (2011).
- [9] L. Bayarjargal, L. Wiehl, and B. Winkler, Influence of grain size, surface energy, and deviatoric stress on the pressure-induced phase transition of ZnO and AlN, *High Press. Res.* **33**, 642 (2013).
- [10] J. Olsen, L. Gerward, and J. Jiang, High-pressure behavior of nano titanium dioxide, *High Press. Res.* **22**, 385 (2002).
- [11] V. Swamy, A. Kuznetsov, L. S. Dubrovinsky, R. A. Caruso, D. G. Shchukin, and B. C. Muddle, Finite-size and pressure effects on the Raman spectrum of nanocrystalline anatase TiO<sub>2</sub>, *Phys. Rev. B* **71**, 184302 (2005).
- [12] V. Swamy, A. Kuznetsov, L. S. Dubrovinsky, P. F. McMillan, V. B. Prakapenka, G. Shen, and B. C. Muddle, Size-dependent pressure-induced amorphization in nanoscale TiO<sub>2</sub>, *Phys. Rev. Lett.* **96**, 135702 (2006).
- [13] L. Huston, A. Lugstein, G. Shen, D. Cullen, B. Haberl, J. Williams, and J. Bradby, Synthesis of novel phases in Si nanowires using diamond anvil cells at high pressures and temperatures, *Nano Lett.* **21**, 1427 (2021).
- [14] S. Tolbert, A. Herhold, L. Brus, and A. Alivisatos, Pressure-induced structural transformations in Si nanocrystals: Surface and shape effects, *Phys. Rev. Lett.* **76**, 4384 (1996).
- [15] Y. Wang, J. Zhang, J. Wu, J. Coffer, Z. Lin, S. Sinogeikin, W. Yang, and Y. Zhao, Phase transition and compressibility in silicon nanowires, *Nano Lett.* **8**, 2891 (2008).
- [16] H. Poswal, N. Garg, S. Sharma, E. Busetto, S. Sikka, G. Gundiah, F. Deepak, and C. Rao, Pressure-induced structural phase transformations in silicon nanowires, *J. Nanosci. Nanotechnol.* **5**, 729 (2005).
- [17] L. Huston, A. Lugstein, J. Williams, and J. Bradby, The high pressure phase transformation behavior of silicon nanowires, *Appl. Phys. Lett.* **113**, 123103 (2018).
- [18] S. Klotz, J. Chervin, P. Munsch, and G. Le Marchand, Hydrostatic limits of 11 pressure transmitting media, *J. Phys. D* **42**, 075413 (2009).
- [19] Z. Dong and Y. Song, Size- and morphology-dependent structural transformations in anatase TiO<sub>2</sub> nanowires under high pressures, *Can. J. Chem.* **93**, 165 (2015).
- [20] O. Degtyareva, M. McMahon, and R. Nelves, High-pressure structural studies of group-15 elements, *High Press. Res.* **24**, 319 (2004).
- [21] D. J. Campbell, D. T. Sneed, E. F. O'Bannon, III, P. Söderlind, and Z. Jenei, Refined room-temperature equation of state of Bi up to 260 GPa, *Phys. Rev. B* **107**, 224104 (2023).
- [22] S. Ono, High-pressure phase transition of bismuth, *High Press. Res.* **38**, 414 (2018).
- [23] M. I. McMahon, O. Degtyareva, and R. J. Nelves, Ba-IV-type incommensurate crystal structure in group-V metals, *Phys. Rev. Lett.* **85**, 4896 (2000).
- [24] M. I. McMahon, O. Degtyareva, R. J. Nelves, S. van Smaalen, and L. Palatinus, Incommensurate modulations of Bi-III and Sb-II, *Phys. Rev. B* **75**, 184114 (2007).
- [25] R. Brugger, R. Bennion, and T. Worlton, The crystal structure of bismuth-II at 26 kbar, *Phys. Lett. A* **24**, 714 (1967).
- [26] H. Iwasaki, J. Chen, and T. Kikegawa, Structural study of the high-pressure phases of bismuth using high-energy synchrotron radiation, *Rev. Sci. Instrum.* **66**, 1388 (1995).
- [27] U. Häussermann, K. Söderberg, and R. Norrestam, Comparative study of the high-pressure behavior of As, Sb, and Bi, *J. Am. Chem. Soc.* **124**, 15359 (2002).
- [28] R. Husband, E. O'Bannon, H.-P. Liermann, M. Lipp, A. Méndez, Z. Konôpková, E. McBride, W. Evans, and Z. Jenei, Compression-rate dependence of pressure-induced phase transitions in Bi, *Sci. Rep.* **11**, 14859 (2021).
- [29] W. Chaimayo, Synthesis and high-pressure structural studies of bismuth nanoparticles, Ph.D. dissertation, The University of Edinburgh, 2013.
- [30] M. F. P. Wagner, A. S. Paulus, J. Brötz, W. Sigle, C. Trautmann, K.-O. Voss, F. Völklein, and M. E. Toimil-Molares, Effects of size reduction on the electrical transport properties of 3D Bi nanowire networks, *Adv. Electron. Mater.* **7**, 2001069 (2021).
- [31] M. Rauber, I. Alber, S. Müller, R. Neumann, O. Picht, C. Roth, A. Schökel, M. E. Toimil-Molares, and W. Ensinger, Highly-ordered supportless three-dimensional nanowire networks with tunable complexity and interwire connectivity for device integration, *Nano Lett.* **11**, 2304 (2011).
- [32] L. Movsesyan, A. W. Maijenburg, N. Goethals, W. Sigle, A. Spende, F. Yang, B. Kaiser, W. Jaegermann, S.-Y. Park, G. Mul, C. Trautmann, and M. E. Toimil-Molares, ZnO nanowire networks as photoanode model systems for photoelectrochemical applications, *Nanomaterials* **8**, 693 (2018).
- [33] M. Toimil-Molares, Characterization and properties of micro- and nanowires of controlled size, composition, and geometry fabricated by electrodeposition and ion-track technology, *Beilstein J. Nanotechnol.* **3**, 860 (2012).
- [34] M. Wagner, K.-O. Voss, C. Trautmann, and M. Toimil-Molares, Three-dimensional nanowire networks fabricated by ion track nanotechnology and their applications, *EPJ Techniq. Instrum.* **10**, 2 (2023).
- [35] T. W. Cornelius, J. Brötz, N. Chtanko, D. Dobrev, G. Mische, R. Neumann, and M. E. T. Molares, Controlled fabrication of poly- and single-crystalline bismuth nanowires, *Nanotechnology* **16**, S246 (2005).

- [36] M. Cassinelli, S. Müller, Z. Aabdin, N. Peranio, O. Eibl, C. Trautmann, and M. Toimil-Molares, Structural and compositional characterization of  $\text{Bi}_{1-x}\text{Sb}_x$  nanowire arrays grown by pulsed deposition to improve growth uniformity, *Nucl. Instrum. Methods Phys. Res. Sect. B* **365**, 668 (2015).
- [37] R. Boehler, New diamond cell for single-crystal x-ray diffraction, *Rev. Sci. Instrum.* **77**, 115103 (2006).
- [38] H.-P. Liermann, Z. Konôpková, W. Morgenroth, K. Glazyrin, J. Bednarčík, E. McBride, S. Petitgirard, J. Delitz, M. Wendt, Y. Bican, A. Ehnes, I. Schwark, A. Rothkirch, M. Tischer, J. Heuer, H. Schulte-Schrepping, T. Kracht, and H. Franz, The extreme conditions beamline P02.2 and the extreme conditions science infrastructure at PETRA-III, *J. Synchrotron Radiat.* **22**, 908 (2015).
- [39] C. Prescher and V. Prakapenka, Dioptas: A program for reduction of two-dimensional x-ray diffraction data and data exploration, *High Press. Res.* **35**, 223 (2015).
- [40] B. Toby and R. Von Dreele, GSAS-II: The genesis of a modern open-source all purpose crystallography software package, *J. Appl. Crystallogr.* **46**, 544 (2013).
- [41] A. Dewaele, F. Datchi, P. Loubeyre, and M. Mezouar, High pressure–high temperature equations of state of neon and diamond, *Phys. Rev. B* **77**, 094106 (2008).
- [42] A. Dewaele, A. Rosa, N. Guignot, D. Andrault, J. Rodrigues, and G. Garbarino, Stability and equation of state of face-centered cubic and hexagonal close packed phases of argon under pressure, *Sci. Rep.* **11**, 15192 (2021).
- [43] R. Angel, M. Alvaro, and J. Gonzalez-Platas, EosFit7c and a Fortran module (library) for equation of state calculations, *Z. Crystal. Mater.* **229**, 405 (2014).
- [44] F. Birch, Finite elastic strain of cubic crystals, *Phys. Rev.* **71**, 809 (1947).
- [45] R. Jeanloz, Universal equation of state, *Phys. Rev. B* **38**, 805 (1988).
- [46] T. Katsura and Y. Tange, A simple derivation of the Birch-Murnaghan equations of state (EOSs) and comparison with EOSs derived from other definitions of finite strain, *Minerals* **9**, 745 (2019).
- [47] J. Gonzalez-Platas, M. Alvaro, F. Nestola, and R. Angel, EosFit7-GUI: A new graphical user interface for equation of state calculations, analyses and teaching, *J. Appl. Crystallogr.* **49**, 1377 (2016).
- [48] S. Li, Z. Wen, and Q. Jiang, Pressure-induced phase transition of CdSe and ZnO nanocrystals, *Scr. Mater.* **59**, 526 (2008).
- [49] Y. Akahama, H. Kawamura, and A. Singh, Equation of state of bismuth to 222 GPa and comparison of gold and platinum pressure scales to 145 GPa, *J. Appl. Phys.* **92**, 5892 (2002).
- [50] L. Liu, H. Song, H. Geng, Y. Bi, J. Xu, X. Li, Y. Li, and J. Liu, Compressive behaviors of bcc bismuth up to 55 GPa, *Phys. Stat. Sol. (B)* **250**, 1398 (2013).
- [51] See Supplemental Material at <http://link.aps.org/supplemental/10.1103/c4fw-p99m> for a comparison of the elastic properties based on various fitting approaches.